Journal of Nuclear Medicine, published on March 20, 2020 as doi:10.2967/jnumed.120.242305

Benefit of improved performance with state-of-the art digital PET/CT for lesion detection in oncology

Suleman Surti[1], Ph.D., Varsha Viswanath[1], B.S., Margaret E. Daube-Witherspoon[1], Ph.D., Maurizio Conti[2], Ph.D., Michael E. Casey[2], Ph.D., and Joel S. Karp[1], Ph.D.

[1]Department of Radiology, University of Pennsylvania, Philadelphia, PA 19104

[2]Siemens Medical Solutions, Knoxville, TN 37932

Corresponding author and reprint requests:

Suleman Surti, Ph.D.
Department of Radiology
Perelman School of Medicine at the University of Pennsylvania
156B John Morgan Building
3620 Hamilton Walk
Philadelphia, PA 19104
Phone: +1 215 573 5460
Fax: +1 215 573 3880
Email: surti@pennmedicine.upenn.edu

Financial Support:
This work was supported by the National Institutes of Health grant Nos. R01-CA113941 and R01-CA196528, and a Siemens research contract

Short title: Lesion detectability with digital PET

ABSTRACT

Latest digital whole-body PET scanners provide a combination of higher sensitivity and improved spatial and timing resolution. We performed a lesion detectability study on two generations of Siemens Biograph PET/CT scanners, the mCT and Vision, to study the impact of improved physical performance on clinical performance. Our hypothesis is that the improved performance of the Vision will result in improved lesion detectability, allowing shorter imaging times or equivalently, lower injected dose. **Methods:** Data were acquired with the Society of Nuclear Medicine and Molecular Imaging Clinical Trials Network torso phantom combined with a 20-cm diameter cylindrical phantom. Spherical lesions were emulated by acquiring spheres-in-air data, and combining it with the phantom data to generate combined datasets with embedded lesions of known contrast. Two sphere sizes and uptakes were used: 9.89 mm diameter spheres with 6:1 (lung) and 3:1 (cylinder) and 4.95 mm diameter spheres with 9.6:1 (lung) and 4.5:1 (cylinder) local activity concentration uptakes. Standard image reconstruction was performed: ordinary Poisson ordered subsets expectation maximization algorithm with point spread function and time-of-flight modeling and post-reconstruction smoothing with a 5 mm Gaussian filter. The Vision images were also generated without any post-reconstruction smoothing. Generalized scan statistics methodology was used to estimate the area under the localization receiver operating characteristic curve (ALROC). **Results:** Higher sensitivity and improved TOF performance of Vision leads to reduced contrast in the background noise nodule distribution. Measured lesion contrast is also higher on the Vision due to its improved spatial resolution. Hence, the ALROC values are noticeably higher for the Vision relative to the mCT. **Conclusion:** Improved overall performance of the Vision provides a

factor of 4-6 reduction in imaging time (or injected dose) over the mCT when using the ALROC metric for lesions ≥ 9.89 mm in diameter. Smaller lesions are barely detected in the mCT, leading to even higher ALROC gains with the Vision. Improved spatial resolution of the Vision also leads to a higher measured contrast that is closer to the real uptake, implying improved quantification. Post-reconstruction smoothing, however, reduces this improvement in measured contrast, thereby reducing the ALROC values for small, high uptake lesions.

Key Words: Lesion detection, LROC, spatial and timing resolution, sensitivity, digital PET.

INTRODUCTION

The first generation of whole-body time-of-flight (TOF) PET/CT scanners, introduced in 2006, achieved a spatial resolution of 4-5 mm with a sensitivity of 5-10 kcps/MBq and system coincidence timing resolution (CTR) in the range of 450-600 ps. The sensitivity was largely determined by the axial field-of-view (AFOV), ranging from 16-21 cm depending on the vendor. The design choice of a 4-5 mm spatial resolution was largely determined by the practical constraints of using photomultiplier tubes (PMTs) in the detector, but also linked together with the sensitivity and acceptable scan times in the clinic. Improved spatial resolution would require a commensurate improvement in sensitivity (or count statistics) to maintain similar image noise levels (*1*). In another study (*2*), however, it was also shown that for high uptake lesions the increased contrast due to improved spatial resolution leads to a reduction in the number of counts needed to produce images of same visual quality. Neither of these studies, however, included the impact of TOF imaging on the resultant images. Recently we performed a detailed simulation study of a modern, fully-3D PET system with iterative image reconstruction using clinically relevant metrics for lesion detection and localization (*3*). We found that for a fixed number of counts and CTR, improved spatial resolution leads to improved contrast measurement and small lesion detectability (*3*).

The last three years have seen the introduction of digital PET/CT systems with higher sensitivity (up to 20 kcps/MBq) due to a longer AFOV and improved CTR (in the range of 210-400 ps) due to the transition from conventional PMTs to silicon PMTs (SiPM) (*4-6*). Some of these systems also have improved spatial resolution due to the use of crystals

that are < 4x4 mm^2 in cross-section (*6*). The overall improved physical performance is expected to translate into a more sensitive and efficient clinical use of these new systems.

When a molecular imaging expert examines a PET image, the goal is to determine whether the image contains abnormal uptake signifying disease. In this study, we used the localized receiver operating curve (LROC) (*7)* to study the gain in observing small lesions produced by the overall performance improvement of the Siemens Biograph Vision compared to the Siemens Biograph mCT. The Biograph Vision provides higher sensitivity due to a longer AFOV, as well as improved spatial resolution and CTR compared to the Biograph mCT (*6,8*). We performed measurements using a heterogeneous torso phantom representing varying attenuation and activity distributions as in a real patient. Ideally, one would like to measure the ability of human observers to correctly identify lesions in a series of images, a task that is formidable given the number of images needed to produce an accurate measurement. Alternatively, automated numerical methods have been developed *(7, 9-11)* and we chose one to serves as a proxy for a molecular imaging expert's detection and localization task (*9*). The area under the localized receiver operating characteristic curve (ALROC), which represents the probability of correctly detecting and localizing a lesion, was calculated as a function of imaging time. The noise in the image can mimic small lesions thus producing false positives. In the case of no noise, the observer would be correct every time and the ALROC would be unity. As noise increases, the observer's ability to correctly identify lesions decreases thus producing a lower ALROC. By comparing results for varying imaging times, we were able to quantify the differences between the two scanners as a difference in sensitivity for this task.

MATERIALS AND METHODS

Scanner Description

All imaging was performed on the Siemens Biograph mCT Flow (*8*) and Siemens Biograph Vision (*6*) scanners. Table 1 summarizes the important physical characteristics and performance values for these two systems. Data were acquired in list-mode prior to processing.

Phantom

The Society of Nuclear Medicine and Molecular Imaging (SNMMI) Clinical Trials Network (CTN) torso phantom was used (Figure 1). This 30-cm-long phantom consists of a uniform background region and two lung regions filled with Styrofoam beads that emulate the attenuation and activity of human lung (*12*). An additional 20-cm diameter x 30-cm long cylindrical phantom was placed axially below the CTN phantom to act as a uniform liver region. The CTN phantom plus the uniform cylinder act as good surrogates for lung and liver with heterogeneous attenuation and activity uptake. Because the CTN phantom has a 2-inch lip, there is a visible gap between the two phantoms in reconstructed images. The CTN phantom also has several physical lesions present in various regions that were not used for this study.

Data Acquisition

The CTN phantom was filled according to the recommended instructions (*12*). The activity concentration in the CTN phantom and uniform cylinder was 5.2 and 5.3 kBq/cc on the Vision and mCT scanners, respectively. Twenty datasets were acquired using

continuous bed motion (CBM) at a bed speed of 3.0 mm/s on each scanner for a total scan time/dataset of 3 min, covering 54 cm of the phantom.

Data were also collected with 4.95- and 9.89-mm diameter spheres in air filled with 37-74 MBq of activity placed in the central plane at many transverse locations in order to overlap with the phantom. These data were collected for a single bed position in a step-and-shoot (S&S) mode and each acquisition was for t_o=30s. Lesion embedding methodology (*13,14*) (modified as described below) was used to add the sphere-in-air data to the CTN phantom data in order to generate lesion present phantom datasets.

Data Generation and Image Reconstruction

The twenty phantom datasets were merged to produce ten datasets that are equivalent to a total imaging time of 6 min per dataset (equivalent bed speed of 1.5 mm/s). To account for activity decay and changing randoms fraction, the first dataset was merged with the twentieth dataset, second with the nineteenth, and onwards. Each of these ten datasets was also parsed into smaller fractions to produce six imaging times: 6, 3, 2, 1.5, 1, and 0.5 min. These 60 datasets, labelled as CTN phantom background data, represent six imaging times with ten statistical replicates per imaging time.

In each of the 60 background datasets we volumetrically embedded (see below) 37 spherical lesions of a fixed size: 16 in the lung and 21 in the cylinder. Lesion embedding is more practical for producing statistical data replicates and can also be used for generating patient data with a known lesion uptake. Two different lesion sizes were used: 9.89-mm diameter with 6:1 (lung) and 3:1 (cylinder) local activity concentration ratios, and 4.95-mm diameter with 9.6:1 (lung) and 4.5:1 (cylinder) local activity concentration ratios. In

this way two (for two lesion sizes) “lesion” datasets were generated for each of the 60 background datasets.

Standard image reconstruction was performed using the ordinary Poisson ordered subsets expectation maximization algorithm with point spread function (PSF) and TOF modeling, and a 5 mm post-reconstruction Gaussian filter. For mCT data we used 3 iterations with 21 subsets to generate images with 1.85 mm x 1.85 mm x 2.03 mm voxels. For Vision data we used 3 iterations with 5 subsets to generate images with 1.65 mm x 1.65 mm x 1.65 mm voxels. The reconstruction algorithm and the number of iterations and subsets used are the default parameters recommended by the manufacturer and used clinically at the University of Pennsylvania. However, standard mCT reconstruction uses slightly larger 2.04 mm x 2.04 mm x 2.03 mm image voxels, but we chose this smaller value here in order to be closer to the Vision image voxel size. Also, the current choice of post-reconstruction smoothing for the Vision images was made in our clinic to maintain consistency in qualitative image quality with the mCT, since patients may be scheduled on either scanner in the clinic. In order to better leverage the improved performance of Vision we also reconstructed all Vision data without application of a post-reconstruction smoothing. However, this was not done for the mCT images, since the goal was to adhere to the current clinical practice for this scanner.

Lesion Embedding

For lesion embedding we choose the plane, p, in the phantom CBM sinogram where we want to embed the lesion. A chunk of the phantom data equal in axial length to a single bed position, and centered over plane p, is reconstructed. From this reconstruction, we

obtain the CBM normalization data (N_{CBM}) and the attenuation correction factors (ACF). The count survival probability for sphere data is calculated as $N_{S\&S}/(N_{CBM}*t_o*ACF)$, where $N_{S\&S}$ is the standard S&S mode normalization data. The count survival probability is then used to "correct" the sphere sinogram. The "corrected" sphere sinogram is added to the phantom CBM sinogram centered over plane p to generate a fused sinogram with the embedded lesion (*15*). In order to have a pre-defined sphere activity uptake relative to the background, we first reconstruct a fused sinogram using all the sphere data. This image together with the phantom only image gives the scale factor between the reconstructed image and the original sphere-in-air dataset, which can be used to select the number of sphere-in-air counts needed to represent a pre-defined sphere local uptake ratio in a fused dataset.

Image Analysis

Lesion detectability was numerically estimated using a generalized scan statistics method (*9*). In this method we use two sets of statistical replicate images, with one set comprising the CTN phantom background and the other set comprising the CTN phantom with embedded lesions. Local lesion contrast is calculated over the multiple embedded lesions in the lesion images as the ratio of mean counts in a spherical VOI (same as sphere diameter) to the mean counts in an annular shell around the spherical VOI (inner diameter twice the sphere diameter and shell thickness of 1 cm). The lesion contrast distribution is fitted to a Gaussian function to estimate the lesion contrast (or signal) probability density function (*pdf*) in the lung and cylinder. The local contrast distribution for noise nodules is calculated by scanning the lung and cylinder regions of the CTN phantom background

images and calculating the contrast for each image voxel. The contrast for each image voxel is calculated in a manner analogous to the sphere contrast calculation with VOIs centered over that voxel. The local contrast distribution for noise nodules is then used to estimate the max-scan distribution of the noise nodule contrast (*pdf* of highest contrast noise nodules present in the background), separately for the lung and uniform cylinder as described in (*9*). The two *pdfs* (signal and noise) for each region are then used to calculate the LROC curve (*7*) from first principles. ALROC values were calculated for each lesion size and lesion location, as well as for all six imaging times, for the mCT and Vision. The error in the ALROC value was determined as the standard deviation of the results over 100 bootstrapped copies obtained from each of the two *pdf*s. The local lesion contrast value averaged over all lesions and its relative standard deviation were also used as measures of accuracy and precision for the lesion uptake measurement.

RESULTS

Figure 2 shows representative reconstructed images that provide a qualitative idea of the impact of scanner performance on lesion detectability as a function of the imaging time.

Figure 3 summarizes the max-scan contrast distribution of background nodules for each sphere size and location. Figure 3A compares results from the Biograph Vision scanner with and without post-reconstruction smoothing. As expected, the max-scan distribution degrades (higher centroid) as the imaging time is reduced and is systematically worse for images without any post-reconstruction smoothing, leading to an increase in false-positive results. The max-scan distribution is also higher for the smaller spheres and

for spheres located in the lung. The change in max-scan centroid as a function of imaging time is larger in the cylinder. In the lung, the max-scan centroid for the longest imaging time for images without post-reconstruction smoothing is higher than the centroid for the shortest imaging time for images with post-reconstruction smoothing. Figure 3B compares esults from the Biograph Vision and mCT scanners, both with post-reconstruction smoothing. Due to lower sensitivity and worse CTR the max-scan centroids are systematically higher for mCT, but they are slightly lower than in Vision without post-reconstruction image smoothing (Figure 3A).

Figure 4 shows measured sphere contrast as a function of imaging time. With post-reconstruction smoothing, both mCT and Vision have very similar measured contrast (although Vision contrast is slightly higher). Without post-reconstruction smoothing, the improved intrinsic spatial resolution of Vision leads to higher measured sphere contrast. Note that despite the higher uptake of the 4.95-mm diameter spheres, the measured contrast is lower than the 9.89-mm diameter spheres due to increased partial volume effect (PVE). However, without post-reconstruction smoothing, PVE is reduced in the images from Vision with a larger relative effect on the smaller spheres.

Figure 5 shows the ALROC calculated as a function of imaging time. In the cylinder and lung, mCT has systematically lower ALROC due to a lower measured sphere contrast and a higher background max-scan contrast distribution relative to Vision with post-reconstruction smoothing. In the cylinder, the ALROC values for Vision with and without post-reconstruction smoothing are very similar. However, in the lung, Vision without post-reconstruction smoothing produces higher ALROC, especially for the 4.95-mm diameter spheres.

Discussion

On the Vision the ALROC value reaches a value of > 0.9 for 9.89-mm diameter spheres in the cylinder after 1 to 1.5 min of imaging versus 6 min on the mCT. The reduced contrast of the 4.95-mm diameter spheres (despite a higher uptake) together with increased max-scan centroid for background nodules leads to lower ALROC relative to the 9.89-mm diameter spheres. However, a 6 min scan will lead to an ALROC of > 0.8 on the Vision. A visual observation of images indicates that, qualitatively, images with ALROC of 0.80 or higher would generally lead to a very high confidence in the lesion detection and localization task. This has been our experience when using this numerical observer in past work as well (*16,17*). In contrast, these spheres are not detectable on the mCT even after 6 min of imaging time (ALROC=0.08).

In the lung, the mCT again underperforms relative to the Vision. The maximum ALROC achieved plateaus at a value < 1.0 for the two sphere sizes and two locations, except for the smaller sphere in Vision without post-reconstruction smoothing where the ALROC continues to increase with imaging time. This is primarily due to the presence of nodular structure in the lung (Styrofoam beads) that leads to an additional non-statistical feature in the max-scan contrast distribution. In the Vision and mCT images with post-reconstruction smoothing the ALROC values for the 9.89-mm diameter sphere are always higher than those for the 4.95-mm diameter sphere due to increased measured contrast and lower max-scan centroid. When comparing the Vision data with and without post-reconstruction smoothing, we find that for the 9.89-mm diameter sphere the ALROC values are similar, limited by the max-scan centroid distribution due to the lung structure.

However, for the 4.95-mm diameter sphere, images without post-reconstruction smoothing show an increase in ALROC, driven primarily by the much higher contrast measured for these spheres. On the Biograph Vision the ALROC reaches a value of ~0.75 for 9.89-mm diameter spheres in the lung after 1 min as opposed to 6 min on the mCT for equivalent ALROC; this is consistent with the reduction in imaging time we observe for the same size spheres in the cylinder. The 4.95-mm diameter spheres are once again barely detectable in mCT with an ALROC of 0.23 after 6 min, which is similar to or worse than those achieved on the Vision scanner after 0.5 min.

The combination of improved spatial resolution, which provides higher measured contrast, and higher intrinsic sensitivity and improved CTR, which result in better noise characteristics (lower max-scan centroid), leads to a significant increase in ALROC for the Vision relative to the mCT. For the Biograph Vision, post-reconstruction smoothing degrades spatial resolution and lowers measured contrast (similar to mCT) but improves noise properties relative to no post-reconstruction smoothing. Generally, the trade-off results in no significant change in ALROC for the 9.89-mm diameter spheres. However, reduced PVE for smaller spheres on the Vision without any post-reconstruction smoothing, leads to a much higher measured contrast. In the case of high uptake small spheres such as those modeled here in the lung, this leads to a distinct gain in ALROC over Vision images with post-reconstruction smoothing.

The improved physical performance of the Biograph Vision leads to a factor of 4-6 reduction in overall scan time for comparable detectability when using ALROC as the metric for 9.89-mm diameter spheres, and larger reduction for 4.95-mm diameter spheres. These results are consistent with past simulation work (*3*) where we estimated a similar

reduction in imaging times for a scanner with improved spatial resolution and CTR and accounting for the 50% higher sensitivity of the Vision relative to the mCT. The improved imaging capability of the Biograph Vision can be utilized to obtain the same image performance with shorter imaging times (or reduced injected dose). Alternatively, the noticeable gains in detection of smaller spheres, that are not visible in mCT, may lead to improved clinical diagnostic capabilities for small lesions, not achievable on the Biograph mCT.

The measured contrast in Biograph Vision without post-reconstruction smoothing is also higher and closer to the real uptake, indicating potential for improved quantification. Hence, these results indicate an advantage to not using any post-reconstruction smoothing on Vision data. This could be extrapolated to conclude that it is likely that mCT performance could also be improved without any post-reconstruction smoothing, albeit for larger sphere. However, this was not tested here since the goal was to adhere to the current clinical practice for this scanner.

Recently we have seen the development of two long axial FOV scanners, the uExplorer (*18*) (better spatial resolution and worse timing resolution than the Vision) and PennPET Explorer (*19*) (closer in both spatial resolution and timing resolution to the Vision). The longer axial length of these systems leads to about a factor of three gain in sensitivity over the Vision for imaging single organs. This gain should lead to better detectability for similar scan times.

Our study used the CTN torso phantom with a uniform cylinder as a surrogate for patient data. While it does not include some of the real-world effects, such as respiratory motion, it does include heterogeneous activity and attenuation regions. Respiratory motion

will add additional blurring in the lung lesions and reduce any advantage of the improved spatial resolution of the Vision. However, the higher sensitivity and CTR will still improve the ALROC performance. There are some additional limitations of this study arising due to the phantom construction: the lung beads are not the same as real lung structure and real liver is not completely uniform as is the cylinder. The methods used in our work are easily applicable to patient datasets with embedded spheres as recently used by us in a different study (*17*). In the future we can envision expanding the current work in that direction. Finally, the embedded spheres had fixed sizes and local activity ratios, while lesions in patients can vary widely in size, shape, and intensity. However, our results show clear gains in ALROC achieved by the Vision scanner, beyond those one would predict from the increased sensitivity (x 1.5) and improved CTR (x 3.0) even for the 9.89-mm diameter spheres. Hence, the improved spatial resolution leads to higher ALROC, especially in smaller lesions.

Our study used a fixed number of iterations for image reconstruction as defined by the vendor. For iterative reconstruction algorithms the image will change as a function of iteration number and hence can impact the ALROC results. However, for this work our aim was to study the impact of the scanner performance on ALROC results using commercially implemented reconstruction algorithms. In the future we may consider a more in-depth study that investigates the impact of varying reconstruction algorithm parameters to better optimize the scanner performance.

CONCLUSION

Based on our results we conclude that the improved overall performance of the Vision will lead to factor of 4-6 reduction in imaging time (or injected dose) compared to the mCT when using the ALROC metric for lesion detection and localization of spheres ≥ 9.89-mm in diameter. The relative gains for detecting smaller lesions are much larger than this, since the ALROC values are very low on the mCT even for the longest scan time considered here (6 min for imaging 54 cm of phantom length). The improved spatial resolution of the Biograph Vision also leads to a much higher measured contrast that is closer to the known uptake ratio, indicating improved quantification due to reduced PVE. Using post-reconstruction smoothing with a 5 mm Gaussian filter reduces the quantification accuracy in the Vision images and reduces ALROC values for small, high uptake lesions.

DISCLOSURE

This work was supported by the National Institutes of Health grant Nos. R01-CA113941 and R01-CA196528, and a Siemens research agreement with the University of Pennsylvania. Maurizio Conti and Michael E. Casey are employees of Siemens Medical Solutions. No other potential conflicts of interest relevant to this article exist.

ACKNOWLEDGMENTS

We would also like to thank Janet Reddin and Joshua Scheuermann (Radiology, University of Pennsylvania) for help with planning and acquisition of the datasets.

KEY POINTS

QUESTION: How do improved spatial and timing resolution in addition to higher sensitivity of modern digital PET/CT impact oncologic lesion detection?

PERTINENT FINDINGS: Task based evaluation of small lesion detection and localization was performed in a heterogeneous SNMMI CTN phantom. Results indicate up to a factor 6 gain in performance with the Biograph Vision scanner relative to Biograph mCT. In addition 5 mm diameter lesions have very low detectability in the mCT for current clinical imaging times, but they are easily detected with the Vision.

IMPLICATIONS FOR PATIENT CARE: The overall improved performance of the Biograph Vision will leads will lead to improved diagnostic capability in patients for detecting small lesions with much shorter imaging times.

REFERENCES

1. Budinger TF, Derenzo SE, Gullberg GT, Greenberg WL, Huesman RH. Emission computer-cssisted comography with single-photon and positron-annihilation photon emitters. *J Comput Assist Tomogr.* 1977;1:131-145.

2. Muehllehner G. Effect of resolution improvement on required count density in ECT imaging - a computer simulation. *Phys Med Biol.* 1985;30:163-173.

3. Surti S, Shore AR, Karp JS. Design study of a whole-body PET scanner with improved spatial and timing resolution. *IEEE Trans Nucl Sci.* 2013;60:3220-3226.

4. Zhang J, Maniawski P, Knopp MV. Performance evaluation of the next generation solid-state digital photon counting PET/CT system. *EJNMMI Res.* 2018;8:97.

5. Pan T, Einstein SA, Kappadath SC, et al. Performance evaluation of the 5-Ring GE Discovery MI PET/CT system using the national electrical manufacturers association NU 2-2012 Standard. *Med Phys.* 2019;46:3025-3033.

6. van Sluis J, de Jong J, Schaar J, et al. Performance characteristics of the digital Biograph Vision PET/CT system. *J Nucl Med.* 2019;60:1031-1036.

7. Swensson RG. Unified measurement of observer performance in detecting and localizing target objects on images. *Med Phys.* 1996;23:1709-1725.

8. Jakoby BW, Bercier Y, Conti M, Casey ME, Bendriem B, Townsend DW. Physical and clinical performance of the mCT time-of-flight PET/CT scanner. *Phys Med Biol.* 2011;56:2375-2389.

9. Popescu LM, Lewitt RM. Small nodule detectability evaluation using a generalized scan-statistic model. *Phys Med Biol.* 2006;51:6225-6244.

10. Barrett HH, Yao J, Rolland JP, Myers KJ. Model observers for assessment of image quality. *Proc Natl Acad Sci.* 1993;90:9758-9765.

11. Gifford HC, Kinahan PE, Lartizien C, King MA. Evaluation of multiclass model observers in PET LROC studies. *IEEE Trans Nucl Sci.* 2007;54:116-123.

12. Ulrich EJ, Sunderland JJ, Smith BJ, et al. Automated model-based quantitative analysis of phantoms with spherical inserts in FDG PET scans. *Med Phys.* 2018;45:258-276.

13. Surti S, Scheuermann J, El Fakhri G, et al. Impact of time-of-flight PET on whole-body oncologic studies: a human observer lesion detection and localization study. *J Nucl Med.* 2011;52:712-719.

14. Daube-Witherspoon ME, Surti S, Perkins AE, Karp JS. Determination of accuracy and precision of lesion uptake measurements in human subjects with time-of-flight PET. *J Nucl Med.* 2014;55:602-607.

15. Panin VY, Smith AM, Hu J, Kehren F, Casey ME. Continuous bed motion on clinical scanner: design, data correction, and reconstruction. *Phys Med Biol.* 2014;59:6153-6174.

16. Surti S, Karp JS. Impact of detector design on imaging performance of a long axial field-of-view, whole-body PET scanner. *Phys Med Biol.* 2015;60:5343-5358.

17. Viswanath V, Daube-Witherspoon ME, Karp JS, Surti S. Numerical observer study of lesion detectability for a long axial field-of-view whole-body PET imager using the PennPET Explorer. *Phys Med Biol.* 2020;65:035002.

18. Badawi RD, Shi H, Hu P, et al. First Human Imaging Studies with the EXPLORER Total-Body PET Scanner. *J Nucl Med.* 2019;60:299-303.

19. Karp JS, Vishwanath V, Geagan M, et al. PennPET Explorer: Design and Preliminary Performance of a Whole-body Imager. *J Nucl Med.* 2020;61:136-143.

Table 1: Summary of physical characteristics and relevant performance metrics of the two Siemens PET/CT scanners used in this study.

	Biograph mCT Flow *(8)*	Biograph Vision *(6)*
Detector	PMT-based analog	SiPM-based digital
Scintillator	4x4x20mm^3 LSO	3.2x3.2x20mm^3 LSO
Axial FOV (cm)	21.0	26.3
NEMA spatial resolution @ 1-cm (mm)	4.2	3.6
Coincidence timing resolution (ps)	538	215
NEMA sensitivity (kcps/MBq)	10.0	15.6

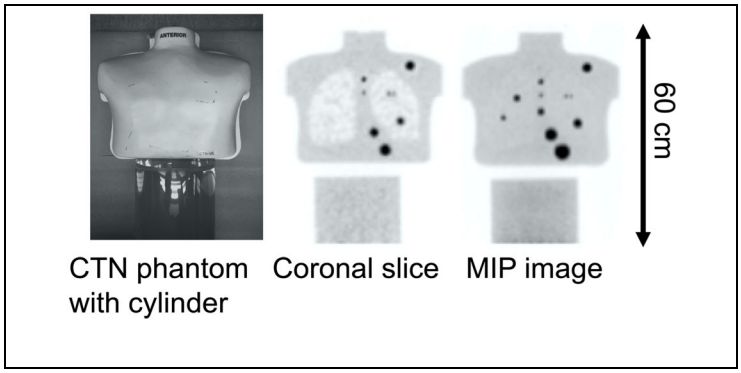

Figure 1

Figure 1: (Left) Picture of the SNMMI CTN torso phantom together with a 20 cm diameter x 30 cm long cylinder used for these measurements. Sample reconstructed coronal (Middle) and a maximum intensity projection (MIP) (Right) images are also shown. There is a lip at the bottom of the CTN phantom and at the top of the cylinder that shows up as the gap between in the reconstructed images. The spheres visible in these images are the physical spheres that are part of this phantom and were not used for the detectability study here.

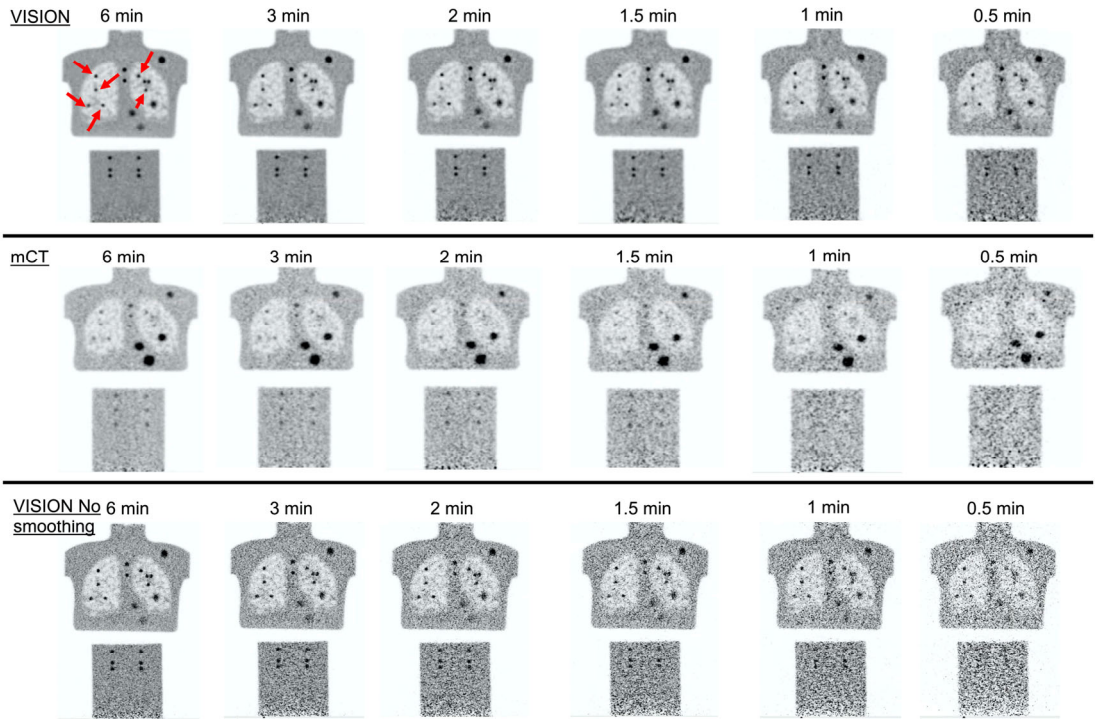
VISION
6 min
3 min
2 min
1.5 min
1 min
0.5 min
mCT
6 min
3 min
2 min
1.5 min
1 min
0.5 min
VISION No smoothing
6 min
3 min
2 min
1.5 min
1 min
0.5 min

A

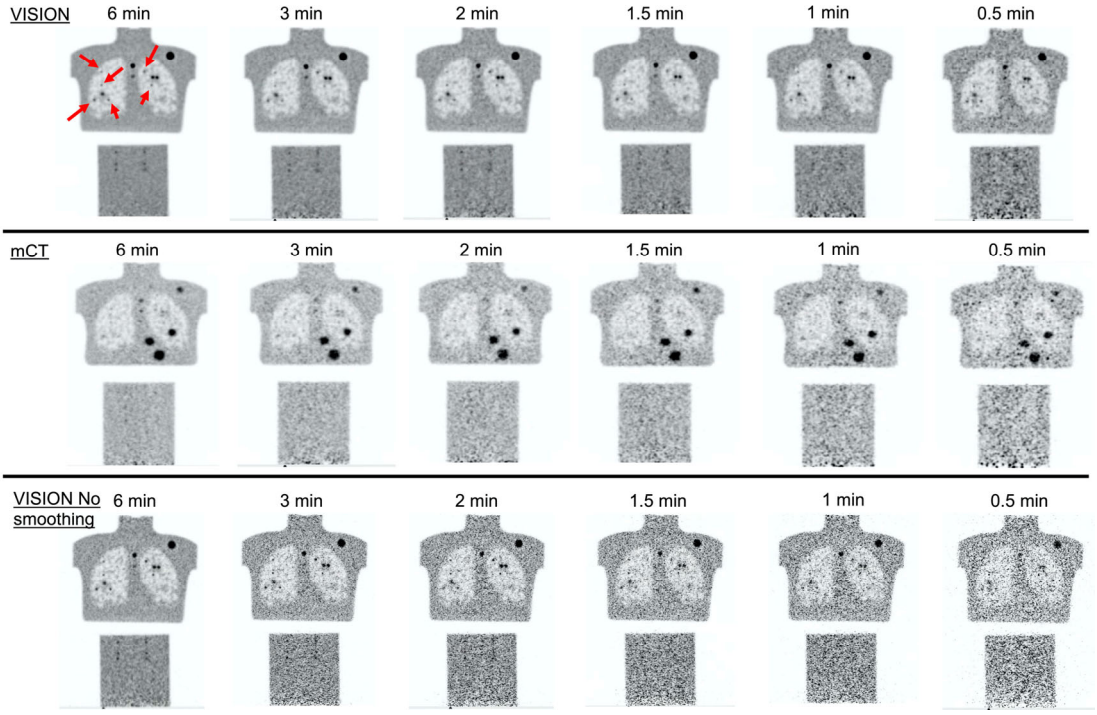
VISION
6 min
3 min
2 min
1.5 min
1 min
0.5 min
mCT
6 min
3 min
2 min
1.5 min
1 min
0.5 min
VISION No smoothing
6 min
3 min
2 min
1.5 min
1 min
0.5 min

B

Figure 2

Figure 2: Coronal slice of example images as a function of imaging time from mCT and Vision scanners. Images showing the (A) 9.89-mm and (B) 4.95-mm diameter spheres. Red arrows show the embedded spheres in the lung; all six embedded spheres in the cylinder at the bottom are the same size as those in the lung. Note that the physical spheres visible in the Vision and mCT images are not identical due to the difference in the coronal slice where the embedded spheres were placed.

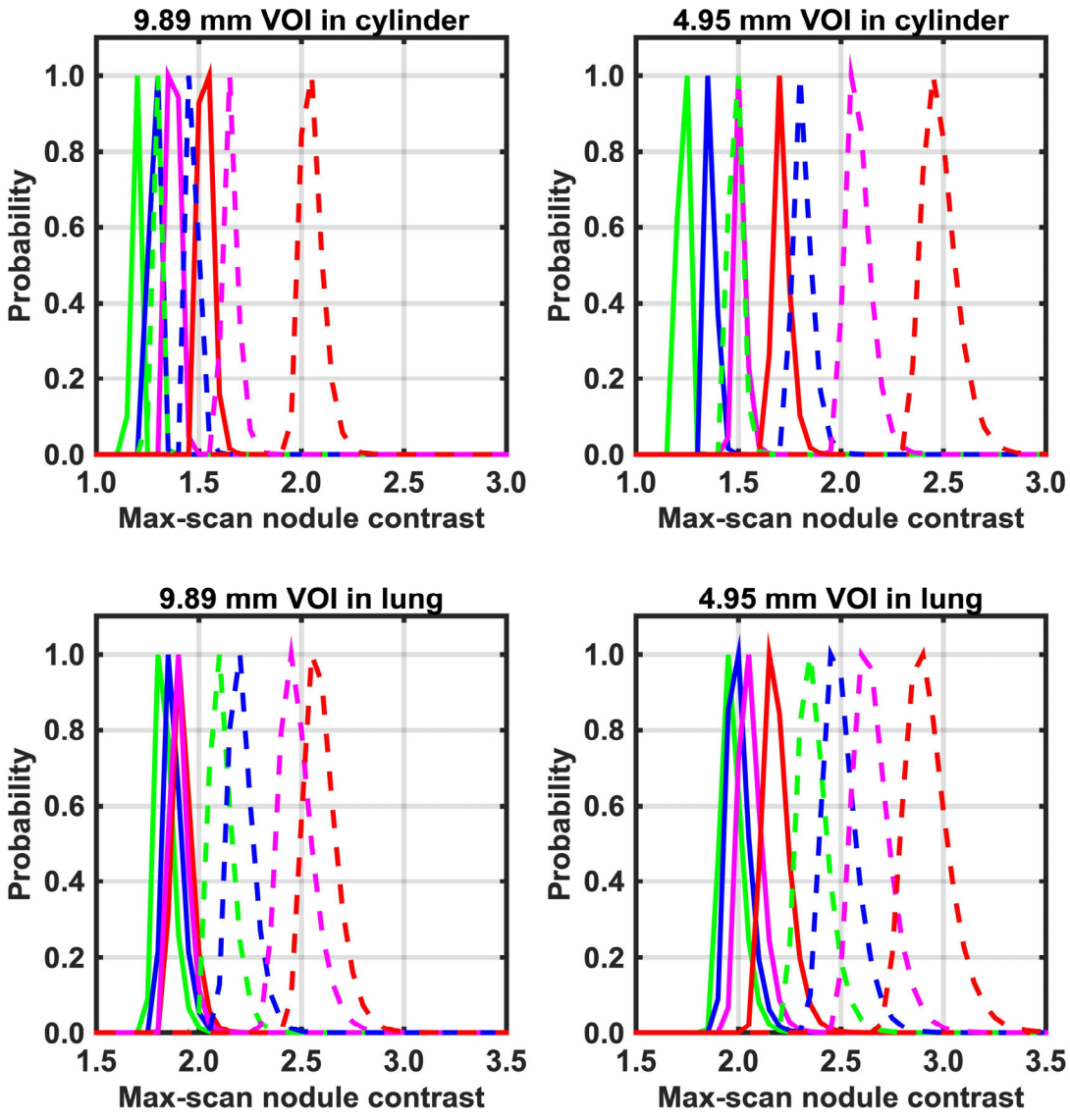
9.89 mm VOI in cylinder
4.95 mm VOI in cylinder
9.89 mm VOI in lung
4.95 mm VOI in lung
Probability
Max-scan nodule contrast
0.0
0.2
0.4
0.6
0.8
1.0
1.5
2.0
2.5
3.0
3.5

A

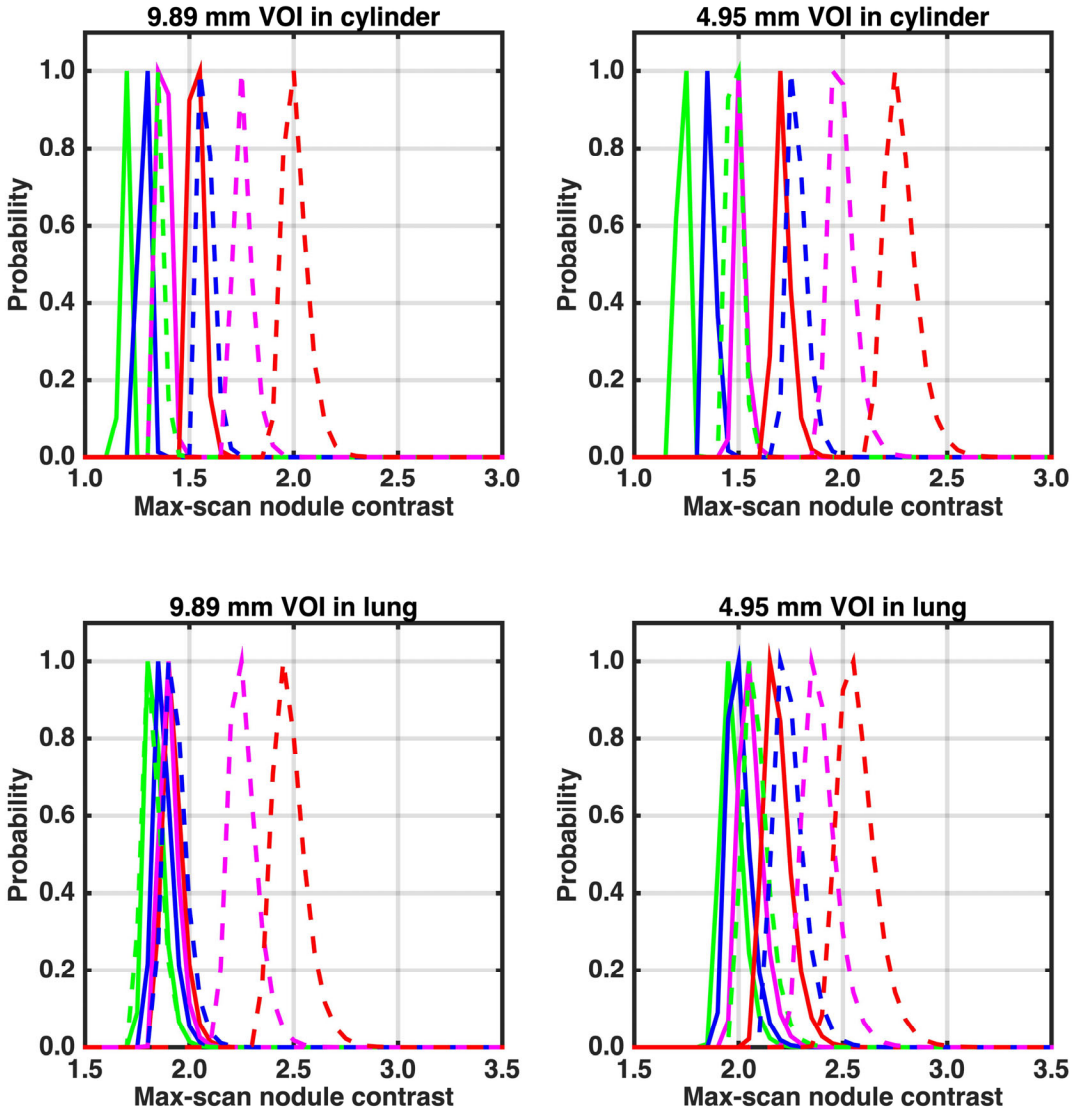

B

Figure 3

Figure 3: The max-scan distribution of the noise nodule contrast calculated in the lung and cylinder regions for 9.89-mm and 4.95-mm diameter spheres. (A) Each plot shows data from the Vision with (solid lines) and without (dashed lines) post-reconstruction smoothing. (B) Each plot shows data from the Vision (solid lines) and mCT (dashed lines), both with post-reconstruction smoothing. Within each group of curves the scan time moving from left to right is 6 (red), 2 (magenta), 1 (blue), and 0.5 (green) min.

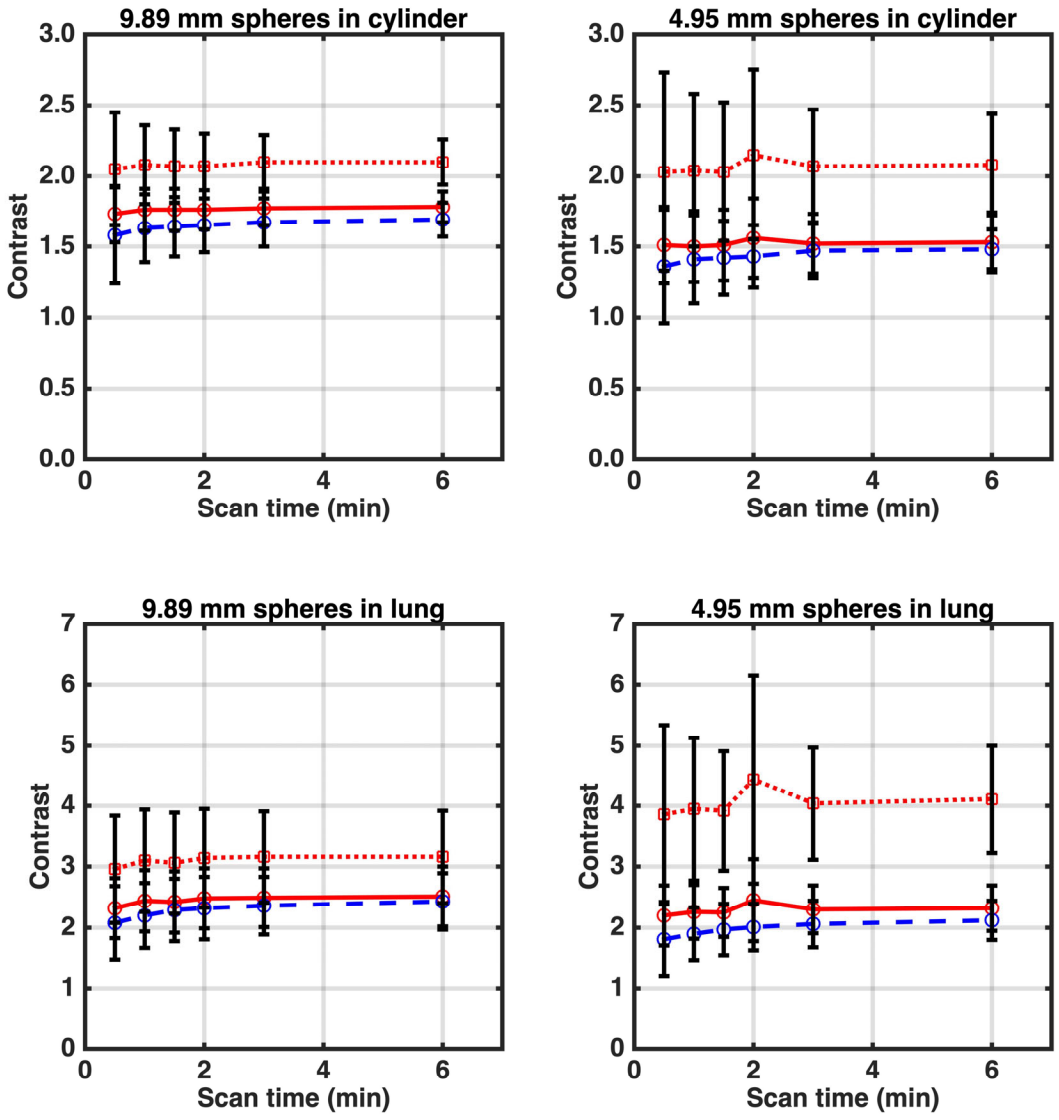

Figure 4

Figure 4: Measured contrast as a function of imaging time for spheres in the lung (bottom) and cylinder (top) regions for 9.89-mm (left) and 4.95-mm (right) diameter spheres. The true activity concentration ratios were 6:1 and 3:1 in the lung and cylinder, respectively, for the 9.89-mm diameter spheres, and 9.6:1 and 4.5:1 in the lung and cylinder, respectively, for the 4.95-mm diameter spheres. The measured contrast values shown here are the mean and the error bars are ± standard deviation calculated over 160 lung spheres and 210 cylinder spheres. The red dotted and solid lines are for the Vision scanner without

and with post-reconstruction smoothing respectively, while the blue dashed line is for the mCT with post-reconstruction smoothing.

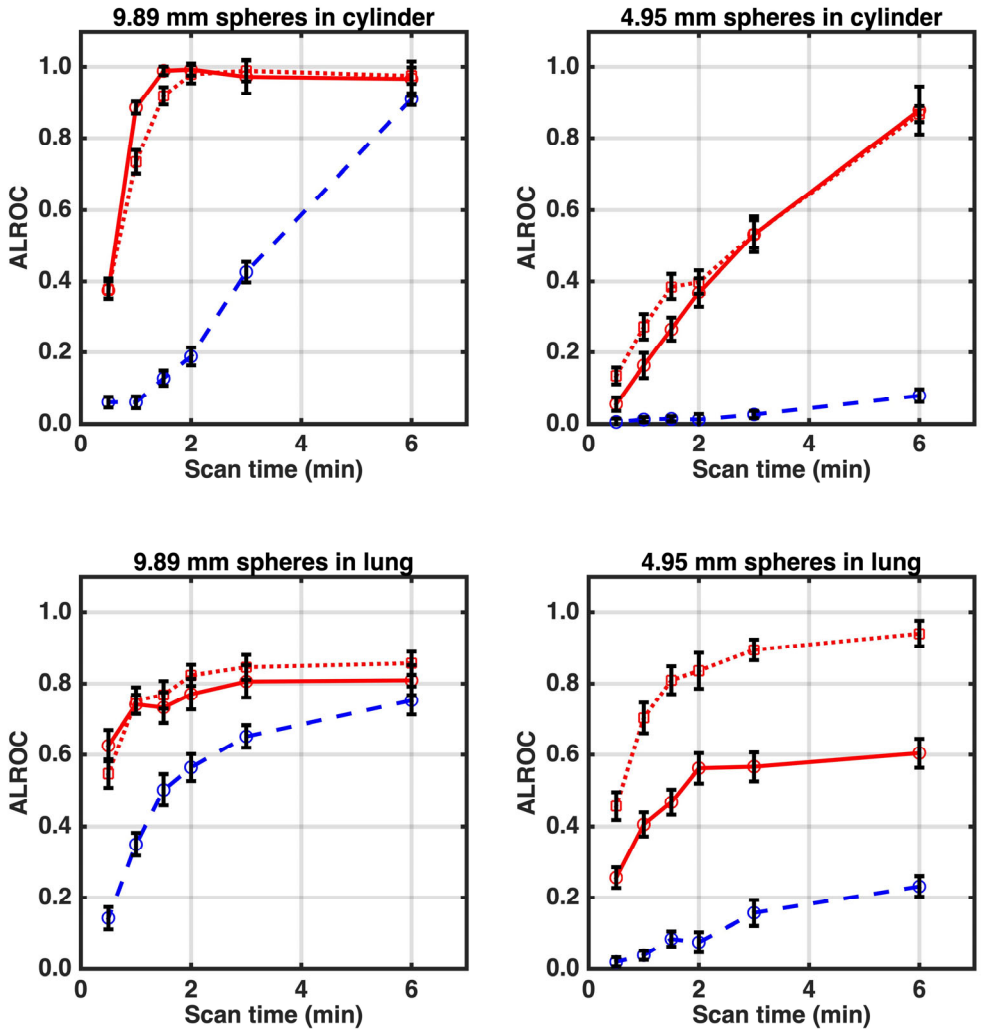

Figure 5

Figure 5: ALROC calculated as a function of imaging time for 9.89-mm (left) and 4.95-mm (right) diameter spheres in the lung (bottom) and cylinder (top) regions. The red dotted and solid lines are for the Vision scanner without and with post-reconstruction smoothing respectively, while the blue dashed line is for the mCT with post-reconstruction smoothing.